

# Selective Localization of Hierarchically Assembled Particles to Plasma Membranes of Living Cells

Asish C. Misra, Tae-Hong Park, Randy P. Carney, Giulia Rusciano, Francesco Stellacci, and Joerg Lahann\*

Particles that preferentially partition to a specific cellular subunit, such as the nucleus, mitochondria, or the cytoskeleton, are of relevance to a number of applications, including drug delivery, genetic manipulation, or self-assembly. Here, hierarchical assemblies of fully synthetic particles that selectively localize to the plasma membrane of mammalian cells are presented. A multimodal approach is used to create assemblies of polymer-based carrier particles with amphiphilic gold nanoparticles immobilized on one hemisphere. These assemblies persist in the plasma membrane of cells for several days and undergo rearrangements and clustering, typically considered to be hallmarks of membrane-bound receptors.

## 1. Introduction

From drug-loaded nanocarriers to prosthetic implants, a number of materials have been designed to interface with biological systems at different length scales.<sup>[1–6]</sup> Of particular

interest is the development of particulate materials that draw their characteristic function from interactions at the cellular and subcellular level, with applications including targeted drug delivery, tissue engineering, or self-assembly.<sup>[7–10]</sup> Nature displays a range of biological structures capable of interfacing with and penetrating through cell membranes, including structures for selective fusion into cellular membranes.<sup>[11–15]</sup>

A number of methods exist for the fabrication of particles with complex architectures which may be used to mimic naturally occurring intricate structures.<sup>[16,17]</sup> For instance, electrohydrodynamic (EHD) cojetting allows for rapid fabrication of particles with complex architectures.<sup>[17–33]</sup> Compared to conventional electro spraying, EHD cojetting involves extrusion of two or more polymer solutions through a nozzle under a laminar flow regime (Figure S1, Supporting Information). Upon application of a DC voltage, the droplet becomes distorted and forms a Taylor cone, from which a high-speed jet is produced.<sup>[34,35]</sup> Modification of process and solution parameters may lead to a variety of bi- and multi-compartmental particles with controllable shape and size.<sup>[21,36]</sup> Due to the laminar flow of the jetting solutions, the interface between solutions is conserved throughout the process leading to the formation of multicompartamental particles.<sup>[21,26,27]</sup>

Because of the establishment of distinct compartments, the particle surface can be chemically modified in ways that lead to distinct patterns.<sup>[19,22,26,29]</sup> Selective surface modification of particle patches has been demonstrated using several different chemistries, including orthogonal click reactions.<sup>[19,29]</sup> A variety of molecules including polymers, dyes, and peptides have been selectively conjugated to a surface patches resulting in directed interactions with mammalian cells.<sup>[26]</sup> Our overarching hypothesis is that an appropriate balance of repulsion and membrane affinity will result in selective localization of hierarchically assembled particles onto plasma membranes.

To tune the interactions of particles with the cell membrane, gold nanoparticles coated with a mixture of 1-octanethiol (OT) and 11-mercaptoundecanesulfonic acid (MUS) are of particular interest because they have previously been reported to penetrate cell membranes through energy-independent pathways.<sup>[37–40]</sup> OT, a hydrophobic ligand, and MUS, a hydrophilic ligand, are organized in a “striped” fashion on the surface of the gold nanoparticles.<sup>[37]</sup> This particular arrangement of ligands affords the particles the ability to penetrate through cell membranes and enter cells without the need for internalization via an endocytic

Dr. A. C. Misra,<sup>[†]</sup> Prof. J. Lahann  
Department of Biomedical Engineering  
University of Michigan  
Ann Arbor, MI 48109, USA  
E-mail: lahann@umich.edu


Dr. T.-H. Park,<sup>[††]</sup> Prof. J. Lahann  
Department of Chemical Engineering  
University of Michigan  
Ann Arbor, MI 48109, USA

Prof. J. Lahann  
Institute for Functional Interfaces  
Karlsruhe Institute of Technology  
76131 Karlsruhe, Germany

Dr. R. P. Carney, Prof. F. Stellacci  
Institute of Materials  
École Polytechnique Fédérale de Lausanne  
1015 Lausanne, Switzerland

Dr. R. P. Carney, Prof. F. Stellacci  
Interfaculty Institute of Bioengineering  
École Polytechnique Fédérale de Lausanne  
1015 Lausanne, Switzerland

Prof. G. Rusciano  
Dipartimento di Fisica “Ettore Pancini” Università di Napoli “Federico II”  
80138 Napoli NA, Italy

 The ORCID identification number(s) for the author(s) of this article can be found under <https://doi.org/10.1002/smt.201800408>.

<sup>[†]</sup>Present address: Department of Surgery, Beth Israel Deaconess Medical Center, Boston, MA 02215, USA

<sup>[††]</sup>Present address: Korea Atomic Energy Research Institute, 111 Daedeok-daero 989beon-gil, Daejeon, Republic of Korea

DOI: 10.1002/smt.201800408

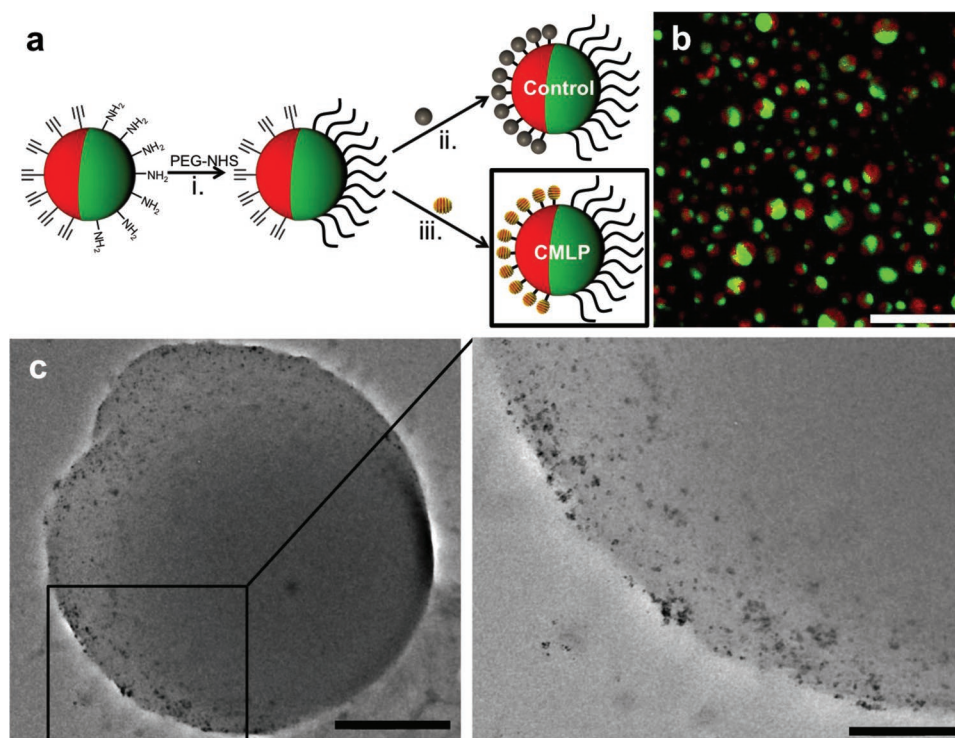


**Figure 1.** Fabrication and characterization of hierarchically assembled particles. a) Design and synthesis scheme of control particles and cell membrane localizing particles, CMLPs. b) Fluorescent CLSM overlay image of CMLPs demonstrating their bicompartamental architecture. Scale bar is 20  $\mu\text{m}$ . c) TEM image of a CMLP (with a magnified image of it on the right), showing selective surface modification with MUS:OT gold nanoparticles on one hemisphere. Scale bars are 500 nm for the left TEM image and 200 nm for the right TEM image.

mechanism.<sup>[37]</sup> This property has been further confirmed by experiments and by theoretical work elucidating the fundamental interactions of these particles with lipid bilayers.<sup>[38,41]</sup> From simulations it has been shown that the gold nanoparticles within the bilayer are a thermodynamically favorable state (minimized exposure of hydrophobic ligands on nanoparticles to water) which is thought to be achieved by stochastic protrusion of an aliphatic lipid tail into solution.<sup>[38]</sup>

In this paper, we use chemically functionalized multicompartamental particles to create carrier systems with two distinct surface patches: i) one hemisphere is modified with polyethylene glycol (PEG) to reduce nonspecific interactions and ii) one hemisphere is decorated with MUS:OT gold nanoparticles to impart affinity toward the plasma membrane of mammalian cells.

## 2. Results and Discussion

First, we prepared bicompartamental particles containing two different chemically reactive polymers that can undergo reactions orthogonal to one another (Figure S1, Supporting Information). The particles were prepared via EHD cojetting of two different polymer solutions of polyacrylamide/poly(acrylic acid) copolymers (PAAm-co-AA) containing PAAm-co-AA modified with acetylene groups<sup>[22]</sup> in one side and dextran modified with amine groups, amino-dextran, in the other. These functional polymers enabled subsequent surface functionalization via chemical coupling reactions. Fluorescein

isothiocyanate (FITC)- and rhodamine-conjugated dextrans were further added to the respective jetting solutions to enable characterization of the particle compartmentalization using confocal laser scanning microscopy (CLSM).<sup>[25]</sup>

The hierarchical assembly of individual particles was achieved by first conjugating PEG onto one hemisphere. For this purpose, amine groups were reacted with *N*-hydroxylsuccinimide-functionalized polyethylene glycol (PEG-NHS). Then, the acetylene groups presented on the second hemisphere were selectively conjugated with azide-functionalized MUS:OT gold nanoparticles via Huisgen 1,3-dipolar cycloaddition. MUS:OT gold nanoparticles, 5 nm in diameter, coated with a 2:1 stoichiometric mixture of OT and MUS were synthesized with a one-phase method.<sup>[37]</sup> Azide-terminated thiol ligands were then place-exchanged on the particles with a protocol that typically leads to  $\approx 10$ – $20$  ligands per particle.<sup>[37]</sup> This surface modification approach resulted in particles that were decorated with MUS:OT gold nanoparticles on one hemisphere and PEG molecules on the remaining hemisphere, denoted as cell membrane-localized particles (CMLPs; **Figure 1a**). The bicompartamental architecture of the particles was intact throughout the surface modification, as confirmed by CLSM (Figure 1b). Since the acetyl-functionalized copolymer and amino-dextran were localized in their respective compartments, the surface-functionalization of these particles was specific, as confirmed by transmission electron microscopy (TEM). TEM images of the fully assembled carrier particles revealed the preferential localization of the gold nanoparticles on one hemisphere (Figure 1c).

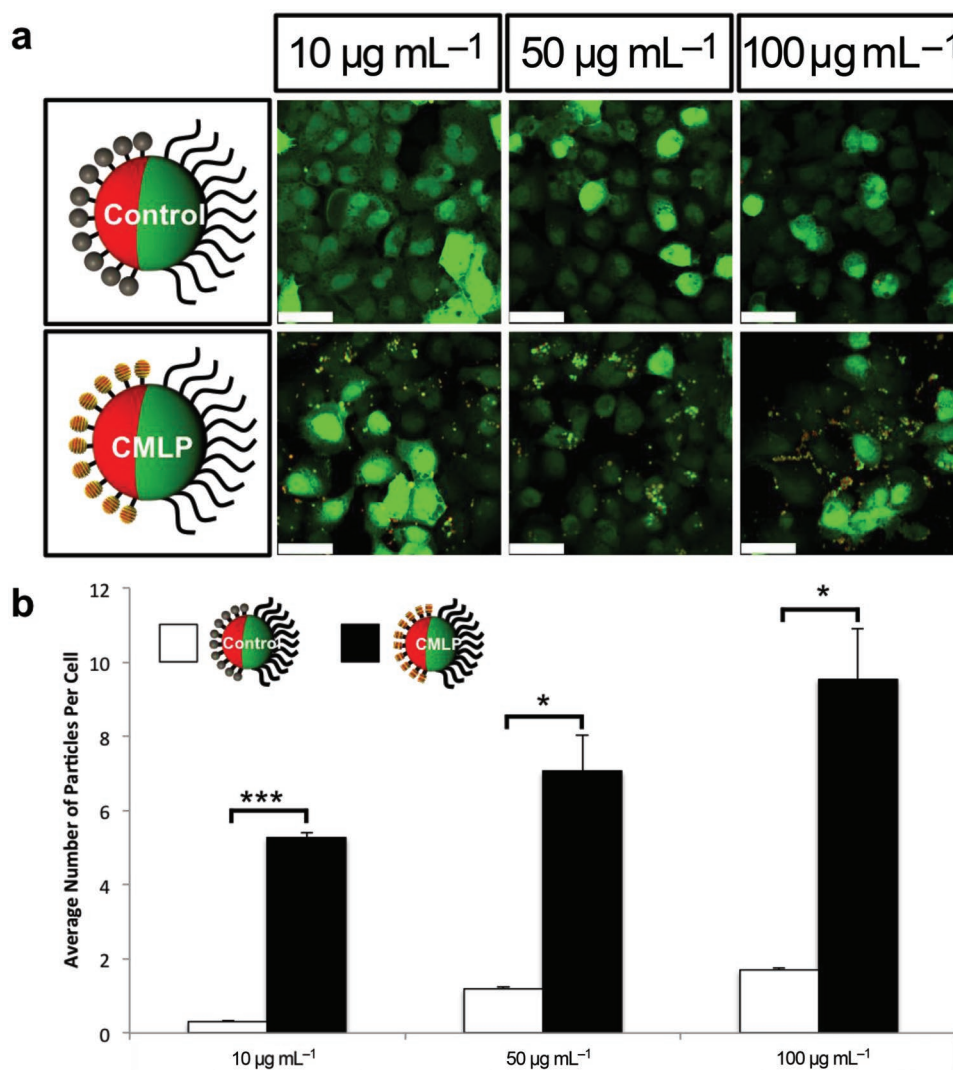


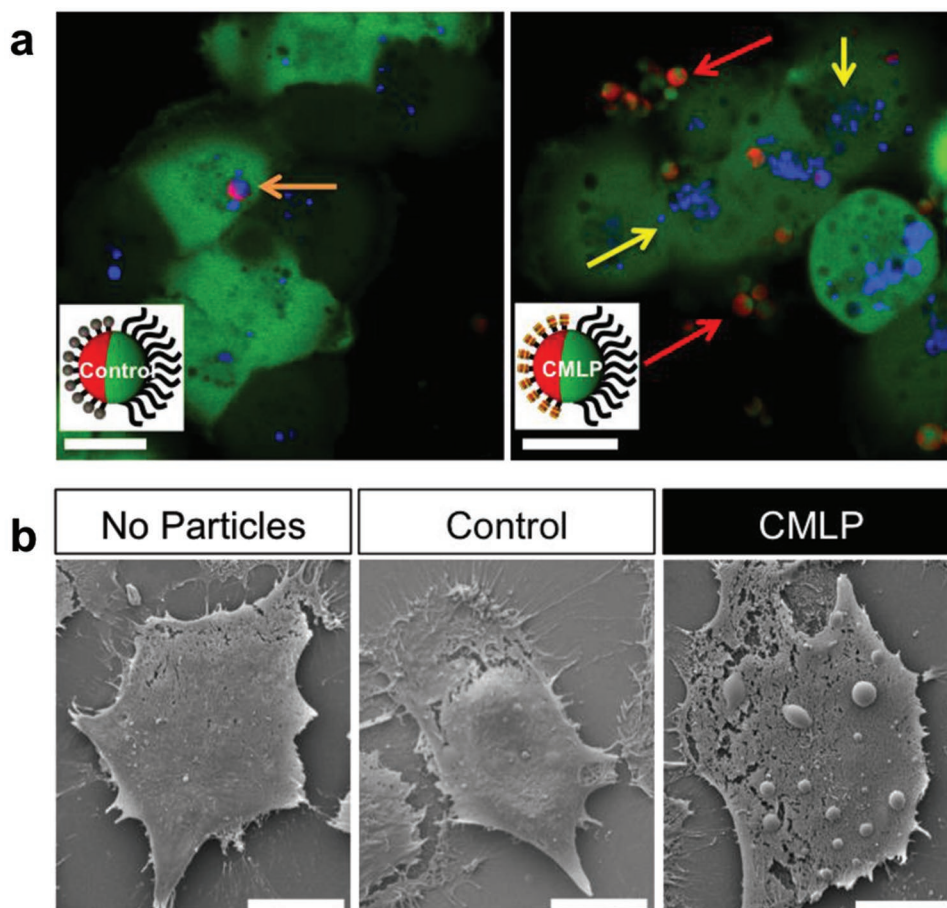
**Figure 2.** Particle incubation with MDA-MB-231/GFP cells. a) Fluorescent CLSM overlay images of MDA-MB-231/GFP cells incubated with control particles and CMLPs for 6 h at concentrations of 10, 50, and 100 µg mL<sup>-1</sup>. Scale bars are 50 µm. b) Quantification of average number of bound and/or internalized particles per cell for 6 h incubation experiments. Significance levels are: \* $p < 0.01$ , \*\* $p < 0.001$ , \*\*\* $p < 0.0001$ .

For comparison, we also synthesized a reference particle, “Control,” (Figure 1a), which was identical to the active particles, CMLPs, except, that the surface-bound gold nanoparticles were coated only with MUS, lacking the unique display of MUS and OT.

To elucidate the in vitro behavior of CMLPs, we incubated breast cancer cells that constitutively express green fluorescent protein, MDA-MB-231/green fluorescent protein (GFP), for 6 h with CMLPs. The CMLPs were compared to the control particles and CLSM analysis was used to assess the cell binding capacity of the particle formulations. Representative images are shown in Figure 2a and reveal that the level of binding was higher for the CMLPs compared to the control particles. Quantification of the number of particles per cell (Figure 2b) suggested that significantly more particles were bound to the cancer cells for the CMLP group than the control group. The maximum binding achieved by the controls was  $1.7 \pm 0.1$  particles per cell for the highest incubation concentration of

100 µg mL<sup>-1</sup>, while  $5.3 \pm 0.1$  CMLPs were bound per cell at the lowest incubation concentration of 10 µg mL<sup>-1</sup>.

To further assess differences in particle internalization, additional studies were performed, staining endosomes with a blue fluorescent dye (LysoTracker) followed by a 6 h incubation.<sup>[42]</sup> This procedure allowed us to identify particles in the cell interior, distinguishing between membrane-bound and endocytosed particles. In Figure 3a, the CLSM images of control particles reveal that the particle fluorescence overlaps with the blue fluorescence from the endosomes (orange arrows), suggesting that these particles are internalized via endocytosis. On the other hand, CMLPs (red arrows) localized outside of endosomes (yellow arrows). Further examination using 3D reconstructions of confocal images verified that the control particles were internalized, while a significant fraction of the CMLPs was localized to the plasma membrane (Figure S2, Supporting Information). These observations were also independently validated by scanning electron microscopy (SEM,



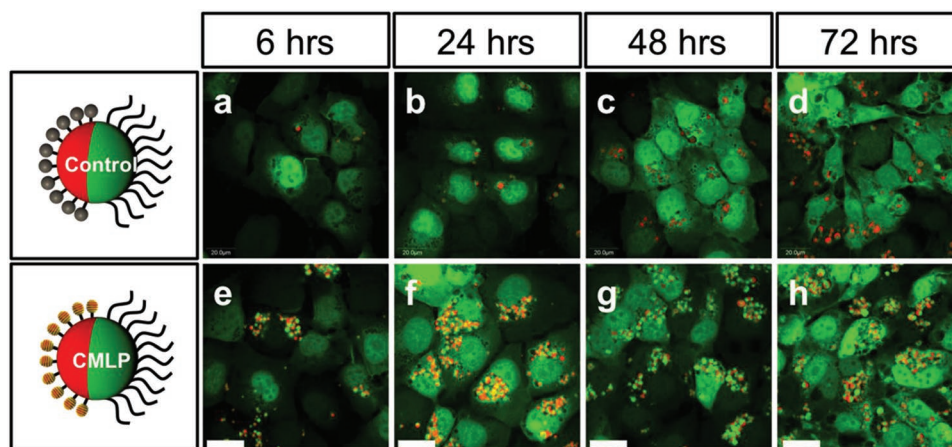
**Figure 3.** Investigation of in vitro binding. a) Fluorescent CLSM images from endosomal staining studies where  $10 \mu\text{g mL}^{-1}$  of particles (red and green) were incubated with MDA-MB-231/GFP cells (green) for 6 h, followed by endosomal staining (blue). Scale bars are  $10 \mu\text{m}$ . b) SEM images of MDA-MB-231/GFP cells after incubation with  $10 \mu\text{g mL}^{-1}$  of particles. Scale bars are  $20 \mu\text{m}$ .

Figure 3b)—for the control, generally one to two particles were found per individual cell surface, whereas as many as ten CMLPs were localized on an individual cell surface. We noted a significant cell-membrane localizing effect associated with the particles with surface-bound amphiphilic gold nanoparticles. This effect may be in part enhanced by markedly reduced nonspecific interactions, primarily endocytosis, by PEGylation, as validated by incubation of unmodified, as-jetted particles and PEGylated particles shown in Figure S3 in the Supporting Information.

Next, we wanted to understand the longer term behavior of the cell membrane binding of CMLPs. We therefore extended the incubation times to 24, 48, and 72 h (Figure 4). At no time point did we observe appreciable cell death, suggesting that these particles were biocompatible under the experimental conditions. Quantification of these data is shown in Figure S4 in the Supporting Information. For incubation times greater than 6 h, we observed that the control particles remained confined in endosomes. From 24 to 72 h, more of the control particles were endocytosed. While we also observed an increase in the endocytosed fraction of CMLPs after 72 h, the majority of the membrane-associated CMLPs rearranged into aggregates that appeared to form specific domains on the cell membrane. To

quantitatively analyze the clustering of CMLPs, a *K*-means analysis was performed based on particle locations determined by red fluorescent confocal images (Figure 5a). There was a fivefold increase of CMLPs found in each cluster compared to the control particles (Figure 5b). Additionally, the average radius of each CMLPs cluster was larger than for the control groups (Figure 5c). The clustering of the CMLPs persisted over the entire period of the experiment revealing a profoundly distinct clustering behavior compared to all control particles. The CMLPs may further associate and cluster on the cell membrane, as it may be a more thermodynamically favorable state. Each CMLP associating to the membrane may decrease the overall binding energy, similar to the receptor clustering of cell membranes.<sup>[43,44]</sup> Hence, CMLPs dispersed in the medium are more likely to bind to these lower energy areas and direct particle clustering over time. However, further studies would be required to demonstrate such a mechanism.

While the exact mechanism of selective localization of CMLPs and their long-term behavior require further studies to elucidate, these current studies suggest that the local interaction of MUS:OT gold nanoparticles with the cellular membrane appears to be a contributory factor. Therefore, to further our understanding of the nature and the effects of such interaction,



**Figure 4.** Longer term behavior. Representative fluorescent CLSM overlay images from long-term incubation studies with (a–d) control particles and (e–h) CMLPs at a fixed concentration of  $100 \mu\text{g mL}^{-1}$ , with incubation times of (a,e) 6, (b,f) 24, (c,g) 48, and (d,h) 72 h. Scale bars are  $25 \mu\text{m}$ .

giant unilamellar vesicles (GUVs),<sup>[45]</sup> typically used to study membrane organization and response to external agents, were employed as a model of cellular membranes. In particular, GUVs based on 1,2-dioleoyl-sn-glycero-3-phosphocholine (DOPC-GUVs), mimicking the fluid phase of real eukaryotic membranes, were used. The study was performed with a Raman-tweezers system, where a Raman microscope was combined with an optical tweezers system,<sup>[46]</sup> that provided access to both the micromechanical and the chemical effect of NPs on the optically trapped GUVs, free from spurious surface-induced artifacts.

Initially, the chemical effect of the MUS:OT gold nanoparticles on the GUVs was investigated. GUVs were studied with the micro-Raman system, after being exposed to different gold nanoparticle concentrations, ranging from  $0.01$  to  $10 \text{ mg mL}^{-1}$ . Above a concentration of  $1 \text{ mg mL}^{-1}$ , a significant number of GUVs spectra exhibited clearly discernable signatures of Raman bands which were attributed to the presence of the MUS:OT gold nanoparticles, as seen in **Figure 6a**. Intriguingly, the intensity changes of these bands among different GUVs appeared to be normally distributed (**Figure 6b**), suggesting a randomized interaction process between nanoparticles and the lipid bilayer,

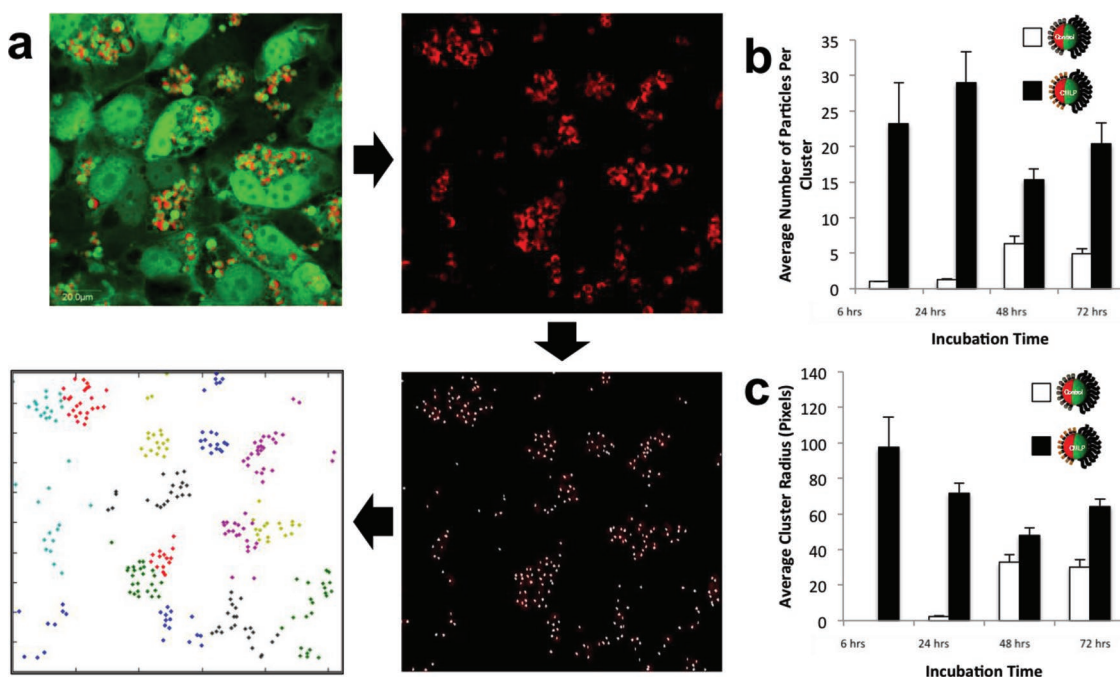


**Figure 5.** Clustering analysis. a) *K*-means clustering analysis of particles at different incubation times, obtained by determining particle position from estimating centers of particles via extracted red fluorescence images. b) Average number of particles per cluster and (c) average cluster radius. Black bars = CMLPs; white bars = control particles. Note average cluster radius for control particles at 6 h is 0 as each cluster contains one particle. Error bars are standard error.

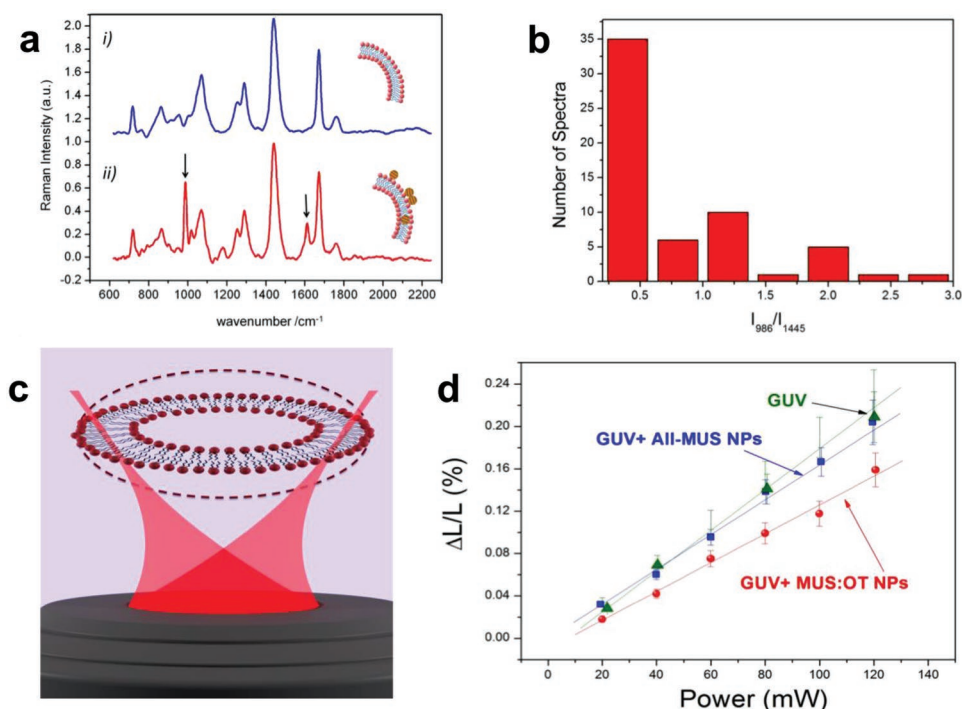


**Figure 6.** Individual gold nanoparticle interactions with GUVs. a) Raman spectra of a single GUV (i) in aqueous solution or (ii) under incubation with MUS:OT NPs at a  $1 \text{ mg mL}^{-1}$  concentration. The arrows in panel (ii) highlight two features related to MUS:OT NPs. b) Statistical distribution of the ratio  $R = I_{986}/I_{1445}$  for 60 GUVs exposed to MUS:OT gold nanoparticles for 3 h. c) Cartoon of the stretching process of a single GUV induced by two optical traps, or tweezers. d) Relative GUV elongation versus optical tweezer laser power for (i) GUVs exposed to MUS:OT gold nanoparticles (MUS:OT NPs), (ii) GUVs exposed to MUS-only gold nanoparticles (All-MUS NPs), and (iii) GUVs in aqueous solution. Errors bars correspond to the standard deviation for measurements on ten GUVs.

which is consistent with their amphiphilic character. This localization effect was not observed for GUVs incubated with gold nanoparticles coated only with MUS, under otherwise identical experimental conditions.

Next, the micromechanical properties of GUVs upon interaction with the amphiphilic gold nanoparticles were investigated. It is known that the insertion of rigid proteins or peptides into membranes typically results in the stiffening of the lipid bilayer.<sup>[47]</sup> In our study, the measurements were performed by capturing a single GUV by a pair of optical tweezers, positioned at two opposite ends of the closed bilayer (Figure 6c). In this configuration, by retaining the GUV, if the position of one optical trap was turned away, the elongation of the trapped GUV was induced. The maximum elongation of GUVs was achieved, when the trapping force, proportional to the trapping beam power, was equal to the GUV's restoring force. Figure 6d reports the maximum relative elongation of GUVs obtained at different trapping laser power upon interaction with the amphiphilic gold nanoparticles as well as for MUS-only gold nanoparticles and for GUV in aqueous condition. The consistently lower elongation with respect to the trapping beam power, as well as the decreased slope, observed in the case of MUS:OT gold nanoparticles suggests that the lipid bilayers of the GUVs are stiffer than GUVs incubated with no nanoparticles. Of note, there was no discernible decrease in elongation of GUVs incubated with MUS-only gold nanoparticles, suggesting that the amphiphilic character of the MUS:OT gold nanoparticles

may play a role in the membrane stiffening. We suspect that in the case of the interaction of a CMLP with a cell, a relatively high local concentration of MUS:OT gold nanoparticles is presented to a portion of the plasma membrane, resulting in a locally stiffened region, which may allow for stabilization of the CMLP on the membrane. Such stabilization may also allow for the clustering phenomenon observed over longer incubation times. Indeed, it has been shown that membrane stiffening can strongly hinder the endocytotic process, or even inhibit it.<sup>[48]</sup> However, the additional PEGylation of one hemisphere of the CMLPs may further contribute to the particular membrane localization observed in this study.

### 3. Conclusion

Our studies were aimed at elucidating the importance of hierarchical surface patterns for particle interactions with plasma membranes in live cells. These particles decorated with MUS:OT gold nanoparticles and PEG exhibited the highest membrane-binding capacity, even at low particle concentrations. The marked differences between CMLPs and control particles suggest selective affinity with plasma membranes which particles displaying standard gold nanoparticles do not have. Based on the GUV experiments, we further speculate that, after CMLPs adhere to the cellular membrane, the interaction of the amphiphilic gold NPs with the lipid bilayer induces a

local stiffening of the cellular membrane itself which, in turn, inhibits the membrane engulfment needed to start the endocytic pathway. With further work, cell membrane-localizing particles (CMLPs) may serve as a novel platform for intracellular delivery of payloads or as a research tool for investigating cell membrane phenomena.

#### 4. Experimental Section

**Materials:** Poly(acrylamide-co-acrylic acid, sodium salts) (PAAm-co-AA) (MW 200 kD, 10% acrylic acid residues) was purchased from Polysciences (PA, USA). Amino dextran (MW 70 kD) was purchased from Molecular Probes (Oregon, USA). Rhodamine B isothiocyanate conjugated dextran (RITC-dextran, MW 70 kD) and fluorescein isothiocyanate conjugated dextran (FITC-dextran, MW 70 kD) were purchased from Sigma-Aldrich. Acetylene-modified PAAm-co-AA was synthesized as described previously.<sup>[22]</sup> Synthesis of azide-functionalized MUS:OT and control gold nanoparticles have been described previously by the Stellacci group.<sup>[21]</sup> MDA-MB-231/GFP cells were obtained from Cell Biolabs, Inc. All cell culture materials were purchased from Invitrogen.

**Fabrication of Bicompartamental Particles:** The preparation of bicompartamental PAAm-co-AA particles was slightly modified from the method previously described.<sup>[25–27]</sup> One solution was prepared by dissolving 50 mg PAAm-co-AA, 10 mg acetylene-modified PAAm-co-AA, and 2 mg of RITC-dextran in 1 mL of H<sub>2</sub>O. The other jetting solution was made by dissolving 50 mg PAAm-co-AA, 10 mg amino-dextran, and 2 mg of FITC-dextran. Both solutions were stirred overnight. The prepared jetting solutions were loaded to two 1 mL syringes and set up side-by-side. A dual channel needle with two 26 gauge tips and 3.25 inch in length (Fibrijets SA-0105, Micromedics, Inc., MN, USA) was connected to the syringes. The flow rates of the two solutions were simultaneously controlled by a single syringe pump (0.2–0.25 mL h<sup>-1</sup>). A voltage around 15–18 kV was applied to the needles using a high potential generator (ES30P, Gamma High Voltage Research, Inc., USA) and the ground was connected to a piece of aluminum foil as a collecting substrate at a 30 cm distance from the end of needle. After EHD cojetting, the particles were thermally crosslinked at 175 °C for 3 h. The final product was collected as a powder.

**Surface Modification of Bicompartamental Particles:** 5 mg of bicompartamental particles and 20 mg of PEG-NHS were added to 0.5 mL H<sub>2</sub>O and the mixture was stirred for 3 h. The suspension was centrifuged and the supernatant was removed. The particles were washed via two cycles of redispersion in fresh water and centrifugation. These particles were freeze dried using a Labconco Freezone 4.5. After the washing procedure, 1 mg of N<sub>3</sub>-functionalized Au NPs (isotropic for control, MUS:OT for CMLP), 0.2 mL of 0.03 M CuSO<sub>4</sub> (aq), and 0.2 mL H<sub>2</sub>O was added to the PEGylated particles. Finally, 20 mg of sodium ascorbate was added and the suspension was agitated for 3 h. The mixture was centrifuged and the supernatant was removed. The residue was washed with water two times, 0.03 M Na<sub>2</sub>EDTA·2H<sub>2</sub>O (aq) three times, and water three times. The functionalized bicompartamental particles were collected after freeze drying.

**Particle Characterization:** An Olympus FluoView 500 CLSM was used to examine the compartmentalized fluorescence distributions of the bicompartamental particles prepared in this study. Ar/ArKr laser ( $\lambda = 488$  nm) and GreNe laser ( $\lambda = 543$  nm) were used to excite FITC and rhodamine B, respectively. The emission wavelength ranges collected were 508–523 nm for FITC and 580–595 nm for rhodamine B. TEM (JEOL 3011) was employed for the microscopic imaging of bicompartamental particles using a copper TEM grid coated with a carbon film (400 meshes, Ted Pella). Cells were imaged by SEM using an AMRAY 1910 Field Emission Scanning Electron Microscope.

**Cell Culture:** MDA-MB-231/GFP cells were grown in Dulbecco's modified Eagle medium supplemented with 10% fetal bovine serum, 1X non-essential amino acids, and 1X penicillin-streptomycin. All in vitro

experiments were performed using cells that had been passaged no more than seven times.

**In Vitro Particle Incubation Experiments:** Cells were seeded at 50 000 cells per well on circular glass slides in 12-well plates and incubated at 37 °C overnight. Media were exchanged with particles in media at a given concentration and incubated at 37 °C for a designated amount of time. After incubation, cells were washed with phosphate buffered saline (PBS) 2–3x, and then fixed with either 4% paraformaldehyde (for confocal) or 2.5% glutaraldehyde (for SEM) for 30 min. For confocal, glass slides were washed with PBS once more, mounted with ProLong Gold, and subsequently imaged using the Olympus CLSM. Triplicate incubations were performed, obtaining confocal images from each incubation—for analysis, incubations were considered where at least 100 cells were analyzed for each condition (for each type of particle and concentration). For SEM, cell samples were prepared after glutaraldehyde fixing by sequential ethanol washing—cells were incubated sequentially with 10%, 30%, 50%, 70%, 90% (2x), and 100% (2x) ethanol in water solutions for 5–10 min at each concentration. Cells were then washed and incubated with hexamethyldisilazane (HMDS); HMDS was exchanged twice after 5–10 min intervals and the final HMDS was allowed to evaporate overnight in a laminar flow hood. Cell samples were then gold sputter-coated and imaged using the AMRAY SEM.

**K-Means Analysis:** The red fluorescence channel images from the incubation experiments, a representative from each concentration and incubation time period, were imported into MATLAB and used to estimate the positions of the particles using `imfindcircles()`. The built-in function `k-means()` was employed to determine *k*-means clustering solutions, and the optimal number of clusters *k* was determined by the *k*-means solution with the highest average silhouette number as given by `silhouette()` (*K*-means was evaluated for the number of clusters from 2 to 25).

**GUV Preparation:** GUVs used for Raman analysis were prepared by electroformation, essentially following the procedure described in ref. [49]. Briefly, DOPC (by Avanti) dissolved in a 10:1 chloroform to methanol solution was spread over the conducting side of an indium tin oxide (ITO) slide and desiccated under reduced pressure. Therefore, a capacitive cell was formed with a second ITO slide and teflon strips acting as spacers. The chamber was finally filled with distilled water and a sine wave (1.5 V, 10 Hz) was applied to the electroformation chamber for 2 h. This procedure produces GUVs which can be stored for up to two weeks at room temperature. For stretching measurements, the electroformation chamber was filled with a 0.3 M sucrose solution and the formed GUVs, filled with the sucrose solution, were diluted into a 0.37 M glucose solution. The refractive index mismatch between sucrose and glucose solutions allows an optimal GUVs imaging under bright field illumination. Moreover, the contrast of the index of refraction across the lipid bilayer allows an efficient optical trapping and pulling of the membrane. For both Raman and stretching measurements, vesicles were selected with a diameter  $\approx 10$   $\mu$ m.

**Raman Tweezers System:** GUV investigation presented herein performed by using a combined Optical Tweezers and micro-Raman system (Raman Tweezers). The setup has been described in detail in ref. [50]. Briefly, it consists essentially in a homemade inverted microscope, endowed with a trapping beam (neodymium-doped yttrium aluminum garnet (Nd:YAG), 1064 nm, Ventus 1064) and a Raman probe at 532 nm (Spectra Physics Millennia Xs). The microscope is equipped with a 100X objective lens (Olympus oil-immersion infinity corrected objective, 1.4 N.A.), in which both lasers are injected through a dichroic mirror. By using a galvomirror, the trapped object is moved across the confocal detection volume of the Raman probe. For stretching measurements, a double-trap system (*optical stretcher*) is set up by applying a square voltage signal at a frequency of 1 kHz to a galvomirror, placed on the optical path of the trapping beam. This allows an easy and optimal control of the relative distance between the two optical traps.

**Raman Measurements on DOPC GUVs:** Raman analysis was performed on DOPC-GUVs incubated for 3 h with MUS:OT NPs. Measurements have been carried out at three different nanoparticles concentrations: 0.01, 0.1, and 1 mg mL<sup>-1</sup>.

From this analysis, it comes out that, starting from a concentration level of 0.1 mg mL<sup>-1</sup>, a significant number of GUVs spectra exhibit new spectral signatures clearly due to MUS:OT NPs, as shown in Figure S4a in the Supporting Information. As a matter of facts, while the spectrum in panel (i) shows spectral features mainly arising from vibrations of the DOPC hydrocarbon chains, the spectrum reported in panel (ii) clearly exhibits new features, mainly around 986 and 1613 cm<sup>-1</sup>, likely due to sulfate and CC bonds in MUS:OT NPs, respectively. However, a high degree of heterogeneity of the acquired spectra shows up, in terms of the relative intensity of bands due to DOPC and MUS:OT NPs. A quantitative description of this process has been obtained by evaluating the ratio  $R = I_{986}/I_{1445}$  of the sulfate band intensity against the DOPC band intensity at 1445 cm<sup>-1</sup> for 60 GUVs exposed to nanoparticles at a concentration of 1 mg mL<sup>-1</sup>. The result is shown in Figure S4b in the Supporting Information. This clearly suggests a random accumulation process of NPs near/inside the lipid bilayer. Importantly, as shown in Figure 6a, the intensity of DOPC Raman features remains reasonably unaffected by NPs addition and NPs-related bands appear to be simply added to the DOPC features, with no evidence of lipid chains destructure typically mirrored, from a spectral point of view, by a reduction in intensity and a broadening of the lipid features. This further supports our evidence of a complete biocompatibility of the amphiphilic gold nanoparticles under the investigated concentration range.

**GUVs Stretching Measurements:** To check the effect of the amphiphilic gold nanoparticles on the micromechanical properties of GUVs, it was proceeded by capturing a single GUV by a pair of OTs, positioned at two opposite ends of the closed bilayer (Figure 6c). Therefore, the distance was increased between the two optical traps up to the maximum extent possible at the given power of the trapping laser. In this condition, the elastic stretching force exerted on the GUVs by the Optical Tweezers balances the GUV restoring force. Therefore, the laser power was increased gradually, proportional to the force applied to the membrane, from 20 to 120 mW. At each step, a GUV image was acquired, successively processed by ImageJ software for the estimation of the GUV relative elongation.

In Figure 6d the relative axial elongation versus the Optical Tweezers laser power was reported for measurements on ten GUVs upon 3 h incubation with MUS:OT nanoparticles (1 mg mL<sup>-1</sup>), incubation with MUS nanoparticles (1 mg mL<sup>-1</sup>) as well as for GUVs in aqueous solution. Clearly, the lower slope obtained for the first case indicates an increase of the apparent membrane stretching constant, and, therefore, a membrane stiffening induced by MUS-OT nanoparticles. On the contrary, interaction with MUS nanoparticles seems not to affect the GUVs mechanical properties (Figure 6d).

## Supporting Information

Supporting Information is available from the Wiley Online Library or from the author.

## Acknowledgements

The authors would like to acknowledge funding from the European Community's Seventh Framework Programme (FP7/2007-2013) under Grant Agreement No. 310445 (SAVVY) and the Defense Threat Reduction Agency (DTRA) for funding provided through grant HDTRA1-15-1-0045. T.-H.P. prepared and characterized all polymeric particles used in the study. The gold nanoparticles were synthesized by R.P.C. A.C.M. performed all in vitro experiments, corresponding confocal and electron microscopy, and K-means analysis. G.R. performed all GUV experiments. The experiments were designed by T.-H.P. and A.C.M., with advice from F.S. and J.L.

## Conflict of Interest

The authors declare no conflict of interest.

## Keywords

nanoparticles, plasma membranes, subcellular targeting

Received: October 12, 2018

Revised: December 11, 2018

Published online: January 28, 2019

- [1] C. D. H. Alarcon, S. Pennadam, C. Alexander, *Chem. Soc. Rev.* **2005**, 34, 276.
- [2] L. Dykman, N. Khlebtsov, *Chem. Soc. Rev.* **2012**, 41, 2256.
- [3] Z. X. Li, J. C. Barnes, A. Bosoy, J. F. Stoddart, J. I. Zink, *Chem. Soc. Rev.* **2012**, 41, 2590.
- [4] X. Y. Liu, P. K. Chu, C. X. Ding, *Mater. Sci. Eng., R* **2004**, 47, 49.
- [5] T. Neuberger, B. Schopf, H. Hofmann, M. Hofmann, B. von Rechenberg, *J. Magn. Magn. Mater.* **2005**, 293, 483.
- [6] M. Niinomi, *Metall. Mater. Trans. A* **2002**, 33, 477.
- [7] K. Cho, X. Wang, S. Nie, Z. G. Chen, D. M. Shin, *Clin. Cancer Res.* **2008**, 14, 1310.
- [8] Z. Nie, A. Petukhova, E. Kumacheva, *Nat. Nanotechnol.* **2010**, 5, 15.
- [9] J. Shi, A. R. Votruba, O. C. Farokhzad, R. Langer, *Nano Lett.* **2010**, 10, 3223.
- [10] K. S. Soppimath, T. M. Aminabhavi, A. R. Kulkarni, W. E. Rudzinski, *J. Controlled Release* **2001**, 70, 1.
- [11] J. Lidmar, L. Mirny, D. R. Nelson, *Phys. Rev. E* **2003**, 68, 051910.
- [12] S. C. Glotzer, M. J. Solomon, *Nat. Mater.* **2007**, 6, 557.
- [13] T. Douglas, M. Young, *Science* **2006**, 312, 873.
- [14] S. C. Glotzer, M. A. Horsch, C. R. Iacovella, Z. L. Zhang, E. R. Chan, X. Zhang, *Curr. Opin. Colloid Interface Sci.* **2005**, 10, 287.
- [15] D. Hoekstra, J. W. Kok, *Biosci. Rep.* **1989**, 9, 273.
- [16] J. Yoon, K. J. Lee, J. Lahann, *J. Mater. Chem.* **2011**, 21, 8502.
- [17] K. J. Lee, J. Yoon, J. Lahann, *Curr. Opin. Colloid Interface Sci.* **2011**, 16, 195.
- [18] A. C. Misra, S. Bhaskar, N. Clay, J. Lahann, *Adv. Mater.* **2012**, 24, 3850.
- [19] S. Saha, D. Copic, S. Bhaskar, N. Clay, A. Donini, A. J. Hart, J. Lahann, *Angew. Chem., Int. Ed.* **2012**, 51, 660.
- [20] K. J. Lee, J. Yoon, S. Rahmani, S. Hwang, S. Bhaskar, S. Mitragotri, J. Lahann, *Proc. Natl. Acad. Sci. USA* **2012**, 109, 16057.
- [21] S. Bhaskar, K. M. Pollock, M. Yoshida, J. Lahann, *Small* **2010**, 6, 404.
- [22] M. Yoshida, K. H. Roh, S. Mandal, S. Bhaskar, D. W. Lim, H. Nandivada, X. P. Deng, J. Lahann, *Adv. Mater.* **2009**, 21, 4920.
- [23] K. H. Roh, J. Lahann, *J. Am. Chem. Soc.* **2007**, 233.
- [24] M. Yoshida, K. H. Roh, J. Lahann, *Biomaterials* **2007**, 28, 2446.
- [25] K. H. Roh, M. Yoshida, J. Lahann, *Langmuir* **2007**, 23, 5683.
- [26] K. H. Roh, D. C. Martin, J. Lahann, *Nat. Mater.* **2005**, 4, 759.
- [27] K. H. Roh, D. C. Martin, J. Lahann, *J. Am. Chem. Soc.* **2006**, 128, 6796.
- [28] K. H. Roh, M. Yoshida, J. Lahann, *Materialwiss. Werkstofftech.* **2007**, 38, 1008.
- [29] S. Bhaskar, K. H. Roh, X. W. Jiang, G. L. Baker, J. Lahann, *Macromol. Rapid Commun.* **2008**, 29, 1973.
- [30] N. K. Sarangi, A. Patnaik, *RSC Adv.* **2014**, 4, 29463.
- [31] Y. Gao, Y. Yu, *J. Am. Chem. Soc.* **2013**, 135, 19091.
- [32] B. H. Li, M. Wang, K. Chen, Z. F. Cheng, G. J. Chen, Z. X. Zhang, *Macromol. Rapid Commun.* **2015**, 36, 1200.
- [33] E. Bartolami, C. Bouillon, P. Dumy, S. Ulrich, *Chem. Commun.* **2016**, 52, 4257.
- [34] A. M. Ganan-Calvo, *Phys. Rev. Lett.* **1997**, 79, 217.
- [35] W. D. Luedtke, U. Landman, Y. H. Chiu, D. J. Levandier, R. A. Dressler, S. Sok, M. S. Gordon, *J. Phys. Chem. A* **2008**, 112, 9628.



- [36] J. Lahann, *Small* **2011**, 7, 1149.
- [37] A. Verma, O. Uzun, Y. Hu, Y. Hu, H. S. Han, N. Watson, S. Chen, D. J. Irvine, F. Stellacci, *Nat. Mater.* **2008**, 7, 588.
- [38] R. C. Van Lehn, M. Ricci, P. H. Silva, P. Andreozzi, J. Reguera, K. Voitchovsky, F. Stellacci, A. Alexander-Katz, *Nat. Commun.* **2014**, 5, 4482.
- [39] Y. S. Yang, R. P. Carney, F. Stellacci, D. J. Irvine, *ACS Nano* **2014**, 8, 8992.
- [40] P. U. Atukorale, Y. S. Yang, A. Bekdemir, R. P. Carney, P. J. Silva, N. Watson, F. Stellacci, D. J. Irvine, *Nanoscale* **2015**, 7, 11420.
- [41] R. C. Van Lehn, P. U. Atukorale, R. P. Carney, Y. S. Yang, F. Stellacci, D. J. Irvine, A. Alexander-Katz, *Nano Lett.* **2013**, 13, 4060.
- [42] J. Panyam, S. K. Sahoo, S. Prabha, T. Bargar, V. Labhasetwar, *Int. J. Pharm.* **2003**, 262, 1.
- [43] D. Bray, M. D. Levin, C. J. Morton-Firth, *Nature* **1998**, 393, 85.
- [44] C. Gajate, F. Mollinedo, *J. Biol. Chem.* **2005**, 280, 11641.
- [45] D. L. Richmond, E. M. Schmid, S. Martens, J. C. Stachowiak, N. Liska, D. A. Fletcher, *Proc. Natl. Acad. Sci. USA* **2011**, 108, 9431.
- [46] K. Dholakia, T. Cizmar, *Nat. Photonics* **2011**, 5, 335.
- [47] M. Schulz, A. Olubummo, W. H. Binder, *Soft Matter* **2012**, 8, 4849.
- [48] M. Saleem, S. Morlot, A. Hohendahl, J. Manzi, M. Lenz, A. Roux, *Nat. Commun.* **2015**, 6, 6249.
- [49] C. Poole, W. Losert, *Methods Mol. Biol.* **2007**, 16, 400.
- [50] A. C. De Luca, G. Rusciano, R. Ciancia, V. Martinelli, G. Pesce, B. Rotoli, A. Sasso, *Opt. Express* **2008**, 16, 7943.